alloys

MDPI

Relationship between Microstructure, Mechanical Properties and Creep Behavior of a Cr-Rich Ferritic Stainless Steel Produced by Laser Powder Bed Fusion

Dennis Karlsson [1,2], Thomas Helander [2], Eleonora Bettini [3], Carl-Johan Hassila [4], Johan Cedervall [5], Martin Sahlberg [1], Peter Harlin [3] and Ulf Jansson [1,*]

[1] Ångström Laboratory, Department of Chemistry, Uppsala University, P.O. Box 523, 751 20 Uppsala, Sweden; dennis.karlsson@alleima.com (D.K.); martin.sahlberg@kemi.uu.se (M.S.)
[2] Kanthal AB, P.O. Box 502, 734 27 Hallstahammar, Sweden; thomas.helander@kanthal.com
[3] Sandvik Additive Manufacturing, 811 81 Sandviken, Sweden; eleonora.bettini@sandvik.com (E.B.); peter.harlin@sandvik.com (P.H.)
[4] Applied Material Science, Department of Engineering Sciences, Uppsala University, 751 20 Uppsala, Sweden; carljohan.hassila@angstrom.uu.se
[5] Department of Materials and Environmental Chemistry, Stockholm University, Svante Arrhenius väg 16 C, SE-106 91 Stockholm, Sweden; johan.cedervall@mmk.su.se
[*] Correspondence: ulf.jansson@kemi.uu.se

Abstract: Additive manufacturing (AM) techniques such as laser powder bed fusion (L-PBF) are rapidly growing due to the inherent design freedom and possibilities to produce components not available with other techniques. This could be utilized in, e.g., the design of new types of heat exchangers in ferritic stainless steels often used for high-temperature applications. Ferritic stainless steels are, however, difficult to weld and could therefore imply obstacles when produced by AM. When establishing the AM-produced alloy in new applications, it is therefore important to increase the understanding of the mechanical properties and high-temperature creep resistance in relation to the unique microstructure and printability. In this study, we have investigated the microstructure of Cr-rich SS446 ferritic stainless steel produced by L-PBF by microscopical and crystallographic techniques. The properties were compared to the conventionally produced tubes. The rapid cooling and reheating during the application of the subsequent powder layers during L-PBF introduces an intriguing microstructure consisting of a ferritic matrix with precipitation of austenite showing a Kurdjumov–Sachs orientation relationship. Characteristic dislocation networks were observed in the L-PBF samples and contributed to the good mechanical properties in the as-built state (more than twice the yield strength of the conventionally produced tube). Furthermore, the creep resistance at 800 °C was superior to the conventionally produced component, suggesting that L-PBF-produced SS446 possesses many advantages regarding production as compared to the conventional route.

Keywords: ferritic stainless steel; SS446; additive manufacturing; laser powder bed fusion; thermodynamic calculations; solidification

1. Introduction

Ferritic stainless steels (FSSs) are Fe–Cr alloys with high Cr contents together with other alloying elements such as Si, Al, Nb or Ti, which stabilize the body-centered cubic (bcc, $Im\bar{3}m$) structure. Stainless steels typically have a Cr content around 10–30 wt.%, where the Cr content is directly related to the corrosion resistance. FSSs are primarily used due to their high yield strength and resistance to stress corrosion cracking, as well as good electrical properties [1,2]. The solubility of C and N is low in the ferrite structure, leading to the possible precipitation of carbides or nitrides, which could be detrimental for the mechanical properties as well as the corrosion resistance due to Cr depletion. Alloying elements such as Nb or Ti may be used to mitigate the depletion of Cr in the ferrite, but

could lead to the formation of other brittle intermetallic phases [3]. Furthermore, the brittle behavior of FSS may be a serious problem in the manufacturing process due to, e.g., crack formation.

Additive manufacturing (AM) is a relatively new technique that has gained significant interest due to its capability to enable the production of complex designs that are not available in techniques such as casting or molding. The AM of metals and alloys is currently used in, for example, the medical, aerospace or automotive industries to produce high-quality components [4]. One of the most well-known AM techniques is laser powder bed fusion (L-PBF), which utilizes a pre-alloyed powder as the feedstock material. L-PBF is seldom used to build components based on FSSs due to the challenges regarding poor weldability, but some reports with promising properties are available [5–10].

In the L-PBF process, a thin powder layer (tens of μm) is applied and selectively melted using a laser according to a digital model. New layers are subsequently added and melted until a three-dimensional geometry is obtained. The process gives rise to rapid heating and cooling in several cycles, as the previously deposited material will be remelted or reheated during the application of the subsequent layers. This will induce residual stresses, which may cause cracking or delamination if exceeding the yield strength of the material [11]. The residual stresses may, however, be reduced by, e.g., alloy design, preheating of the build plate or post-treatment processes such as annealing or hot isostatic pressing (HIP) [12]. Furthermore, secondary phases such as carbides, nitrides or intermetallics may form during the building process and subsequent post-processing steps. These phases may be utilized to improve the properties of the final component, but they could also be detrimental if not carefully controlled. In FSSs containing high amounts of N, Cr_2N may form upon annealing. In addition to reducing the ductility due to its brittle properties, it will contribute to a depletion of Cr in the ferrite and thereby reduce the corrosion resistance [13]. Cr_2N is commonly observed as precipitates in the ferrite grains of duplex stainless steels or at the grain boundaries during solidification as the solubility of N is reduced during cooling [14]. Ti and Nb may be used to stabilize the FSS, avoiding the formation of Cr-rich carbides or nitrides. The addition of Ti has also been shown to be beneficial for the formation of fine-grained microstructures during L-PBF of FSSs by providing heterogeneous nucleation sites during solidification [6,7,9].

AISI SS446 is a ferritic stainless steel with about 23–26 wt.% Cr. This alloy has high strength and excellent corrosion properties at high temperatures and is therefore frequently used in, e.g., heat exchangers [15]. Furthermore, SS446 exhibits a very good creep resistance, which is important in many high temperature applications [16]. Furthermore, it is known that the ductility is deteriorated by welding, suggesting that there may be difficulties in the L-PBF processing of SS446 [15]. Zhang et al. [17] investigated the effect of Cr additions of up to 27 wt.% in pure Fe and could observe a transition from an equiaxed microstructure into coarse columnar grains with increasing Cr content. They did not, however, evaluate the mechanical properties of the material.

The aim of this study was to investigate the relationship between the microstructure and properties of SS446 produced by L-PBF. Thermodynamic calculations were performed to aid in understanding the formed microstructures, including solidification behavior and formation of secondary phases. The results were compared to earlier work on another FSS [7]. Finally, the mechanical properties and creep behavior of the printed components were investigated and compared with conventional tubes of SS446 produced via hot extrusion.

2. Methods

Components of SS446 FSS were produced using an EOS M100 L-PBF system equipped with a 200 W Ytterbium fiber laser with a wavelength of 1035 nm. To find the optimal process parameters, the laser power, scanning speed and hatch distance were varied. For all samples, a pre-alloyed Sandvik's Osprey® SS446 powder was used. The powder was manufactured by vacuum induction melting and subsequent gas atomization using

N$_2$(g). As a last production step, the powder was sized into a particle size distribution of −53 + 15 μm before packaging in an inert gas atmosphere. The powder consisted of spherical-shaped particles, as shown in the SEM image in Figure 1a.
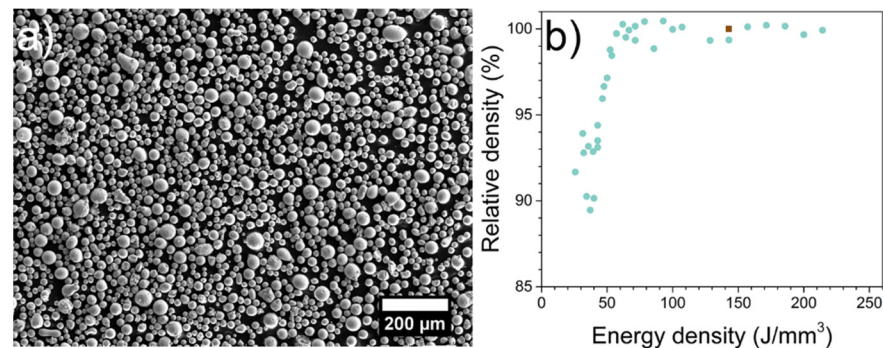

Figure 1. (**a**) SEM image showing the spherical morphology of the feedstock powder and (**b**) relative density of samples built at different process parameters. The brown square shows the relative density of the samples, with a build plate temperature of 200 °C, selected for further studies.

A large number of samples were fused with varying laser power, hatch distance and scan speeds using an unheated build plate. During printing, each layer was segmented into 5 mm wide stripes and melted with a rotational scanning strategy. The density of the fused samples was determined using Archimedes principle in water.

The energy-dependent relative density of all fused SS446 samples is shown in Figure 1b. For all further investigations, the following set of parameters was selected; a laser power of 120 W, a scan speed of 800 mm/s, hatch distance of 70 μm and a 20 μm layer thickness. The sample printed with these process parameters exhibited some cracks, but this was significantly reduced using a build temperature of 200 °C. The relative density of samples built with the selected process parameters was measured to be around 100% by Archimedes principle and is marked with a brown square in Figure 1b. The samples were heat treated at 1060 °C and rapidly quenched in water to room temperature, followed by a second annealing step at 870 °C for one hour and air quenching. Furthermore, tensile test samples, using the selected process parameters, were printed horizontally and vertically. The horizontal samples were printed on a 2 mm support structure to mitigate cracking in the sample due to residual stress between the build plate and the samples.

The chemical composition of the samples printed at the optimized process conditions was analyzed by X-ray fluorescence (XRF) on a XRF PANalytical Magix Fast (Malvern Panalytical, Malvern, UK) according to ASTM E572. The N and O content was analyzed using a LECO TC-600, while the C and S content was analyzed using a LECO CS-600 (Leco Corporation, Sain Koseph, MI, USA) according to ASTM E1019 (ASTM International, West Conshohocken, PA, USA). The composition of the fused material is shown in Table 1. It should be noted that the printed samples contain somewhat less N (0.22 wt.%) compared to the powder (0.26 wt.%). This can be due to a loss of N during the printing process. No significant change in O content was observed in the printed samples compared to the powder.

Table 1. Chemical composition of the powder and L-PBF-produced SS446 ferritic stainless steel in wt.%.

Element	Fe	C	Si	Mn	Cr	Ni	Ti	Al	Nb	N	O
Powder	Bal.	0.11	0.20	0.20	25.70	0.10	N/A	N/A	N/A	0.262	0.021
L-PBF	Bal.	0.082	0.15	0.18	25.73	0.05	<0.01	<0.004	<0.01	0.22	0.022

X-ray diffraction intensities were measured using a Bruker advanced D8 instrument equipped with a Lynxeye position sensitive detector (Bruker Corporation, Billerica, MA, USA). Furthermore, the instrument utilized a monochromator to obtain CuKα_1 radiation with a wavelength of 1.540598 Å. The phase composition and cell parameters were determined using the Rietveld method [18] implemented in the FullProf program [19]. In the refinements, the background was described by linear interpolation between chosen points and the Thompson–Cox–Hastings pseudo-Voigt profile function was used to describe the peak shape. Scale factor, unit cell parameters, peak profile and the background were refined for all phases. For the as-built and heat-treated samples, preferred orientation was refined for the ferritic phase using two preferred directions, namely <001> and <211>.

The microstructure was studied by scanning electron microscopy (SEM) in a Zeiss Merlin (Carl Zeiss, Oberkochen, Germany) equipped with an X-max 100 mm^2 silicon drift energy dispersive X-ray spectroscopy (EDS) detector and a Nordlys max electron backscatter diffraction (EBSD) detector from Oxford Instruments (Abingdon, UK). The EBSD analysis was carried out at an acceleration voltage of 20 kV, electron current of 20 nA at 14 mm working distance. The data were evaluated using the Oxford Instrument HKL Channel 5 software. Prior to analysis, the samples were polished with diamond suspensions and a final polishing step using colloidal SiO$_2$. Lastly, analyses at high magnifications were carried out in a FEI Titan Themis 200 (FEI Company, Hillsboro, OR, USA) scanning transmission electron microscope (STEM) equipped with probe corrector and a SuperX EDS detector (Thermo Fisher Scientific, Waltham, MA, USA). The TEM lamellas were prepared by the in situ lift-out technique in a Zeiss Crossbeam 550 (Carl Zeiss, Oberkochen, Germany) focused ion beam (FIB). The surface was protected by depositing a Pt layer prior to lift-out and a final polishing step using 5 keV ions was used to minimize ion damage.

Both tensile test and creep test rods were machined from the L-PBF samples (from printed samples with a dimension of 10 × 60 × 50 mm^3). Three rods of each condition were turned to a gauge diameter of 4 mm and a gauge length of 24 mm, fulfilling the demands on a ASTM E8M 4c20 test rod. The surface impurities were removed by polishing using a #1200 grit SiC paper. Tensile testing was performed using an Instron 4505 (Instron, Norwood, MA, USA) electromechanical machine with a load capacity of 100 kN. To reduce the time of the test, the initial strain rate was set to 0.00025/s until reaching a strain of 1.7%, whereby the strain rate was increased to 0.005/s until fracture. The test methodology was performed in accordance with ASTM E8M. Creep tests were performed at 800 °C at three different stress levels, namely 8, 9 and 10 MPa on the annealed samples. For the creep testing, a constant-load creep testing machine of in-house Kanthal® (Hallstahammar, Sweden) design was used. The elongation was recorded as a function of time and plotted as creep strain versus time. The stress required for rupture at 1000 h and 10,000 h was estimated by assuming a linear relationship between log (stress) and log (time to rupture), often used in evaluation of creep data [20].

3. Thermodynamic Calculations

Thermodynamic calculations were performed using the Thermo-Calc [21] software (2022a) utilizing the CALPHAD (CALculation of PHAse Diagram) method [22] and the TCFE9 database [23]. The chemical composition of the printed material (Table 1) was used as input. As the solidification process is far from equilibrium in L-PBF due to the high cooling rates (10^4–10^6 K/s [24,25]), the equilibrium phase fraction diagram is not sufficient to describe the segregation in the as-built microstructure. Thereby, calculations utilizing the Scheil–Gulliver model were performed. This model assumes no diffusion in the solid state, and a perfect mixing in the liquid with a local equilibrium at the solid–liquid interface. As light elements such as C and N are in interstitial solid solution, they have a high mobility in the solid state. Thus, a perfect mixing of these elements was assumed in both the liquid and solid phases and they were selected as fast diffusers in the Thermo-Calc software.

The calculated phase fraction diagram can be seen in Figure 2. The ferritic phase (body-centered cubic, bcc) is stable over the entire temperature range in combination with

other phases. At low temperatures (lower than 500 °C), a second bcc phase can be seen in the phase fraction diagram. This is due to the high Cr content, resulting in a miscibility gap in the phase diagram where the single-phase solid solution is not stable, resulting in a phase separation into a Cr-rich α′ phase and a Fe-rich α phase. The phase separation is likely due to spinodal decomposition, commonly seen in Fe–Cr systems with high Cr content. Furthermore, the high Cr content also induces the formation of a σ phase at around 500 °C, which is stable up to 700 °C. As the temperature increases, an austenitic (face-centered cubic, fcc) phase can form between 1000 °C and 1300 °C. The high C and N contents in the SS446 alloy stabilizes the austenitic phase as they are strong austenite stabilizers. This agrees with predictions from a Schaeffler diagram, wherein the phase configuration depends on composition (in terms of Cr equivalents and Ni equivalents), as a duplex-like structure with both bcc and fcc phases present could be expected in the SS446 alloy.
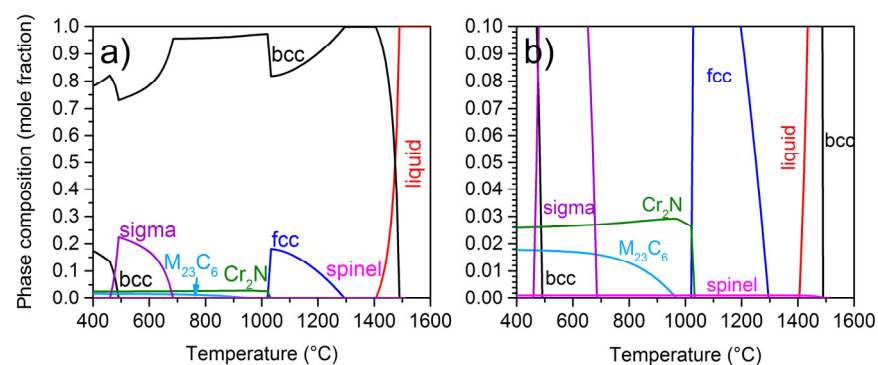

Figure 2. Phase fraction diagram for the SS446 ferritic stainless steel, where (**a**) shows the full phase composition and (**b**) a magnified diagram showing phases with a mole fraction of up to 0.1.

Small amounts of other phases can also form in a wide temperature range. They are seen in Figure 2b, which is a magnified phase fraction diagram showing phases with a mole fraction up to 0.1. As can be seen, carbide ($M_{23}C_6$) and nitride (Cr_2N) are stable in a wide temperature range from low temperatures up to around 1050 °C. At equilibrium, the amount of $M_{23}C_6$ and Cr_2N can be as much as 1.8 and 2.6 mole %, respectively. They are dissolved as the austenitic phase is formed and thus, no carbides or nitrides are expected above a temperature of around 1050 °C. Additionally, small amounts of oxides can be formed due to the presence of O. The thermodynamically stable oxide crystallizes in the spinel structure (AB_2O_4, where A and B are metals) and is present up to 1520 °C. The oxide is stable above the liquidus temperature of the ferrite, and may therefore potentially act as nucleation sites for the solidification of the steel [7].

The solidification pathway was evaluated using the Scheil–Gulliver model and is shown in Figure 3a,b. The first phase to form is the spinel at 1520 °C. The amount of spinel in SS446 is very low (0.02 mole %). When the alloy is cooled further down, the bcc phase will start to solidify around 1490 °C. At the end of the solidification, a small amount of a Cr_2N phase is expected. Figure 3c,d shows the solidification pathway for SS441 from ref. [7]. This alloy consists of a higher Ti content (for full composition, see ref. [13]), enabling the formation of a corundum and TiN phase at temperatures above 1600 °C. It has been shown that the surface of small amounts of a corundum phase or TiN particles can act as nucleation sites and modify the grain structure of other ferritic stainless steels [6,7,9,26]. However, Figure 3 shows that the temperature range and amount of oxides/TiN are very different in SS446 compared to SS441, with a significantly higher amount of possible nucleation sites in SS441.
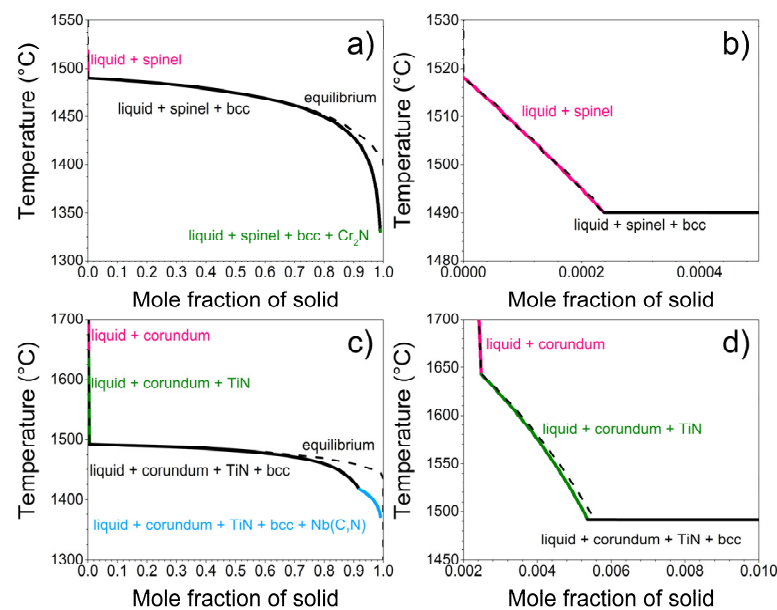
Figure 3. (**a**) Solidification pathway for the SS446 alloy showing presence of spinel, bcc and Cr_2N; (**b**) shows a magnified region of the early solidification from (**a**). (**c**) Shows the solidification pathway of the SS441 alloy and (**d**) a magnified region of the early solidification from (**c**). (**c**,**d**) Are adapted from ref. [7] to facilitate the discussion.

4. Experimental Results and Discussion

Figure 4 shows X-ray diffraction patterns from the feedstock powder, the as-built and post-annealed samples. As can be seen, the powder mainly consists of a ferritic phase (bcc) with random orientation of the crystal grains. In addition to the ferrite, some additional peaks are visible around the bcc {110} peak (Figure 4b). They can be attributed to an austenitic (fcc) phase, which has formed during solidification in the atomization process. The austenitic phase is not expected to form during solidification according to the thermodynamic calculations using the Scheil–Gulliver model shown in Figure 3. The discrepancy can be explained by the observed loss of N during the printing process. N is a strong austenite stabilizer and small variations of the element can have a large effect on the phase composition. The calculations in Figure 3 were based on the composition of the printed samples, shown in Table 1, with 0.22 wt.% N. Calculations with a higher N content of the powder, 0.26 wt.%, (non-published result) yields an fcc phase at the end of the solidification process and could thereby explain the presence of this phase in the powder and to some extent in the as-printed samples.
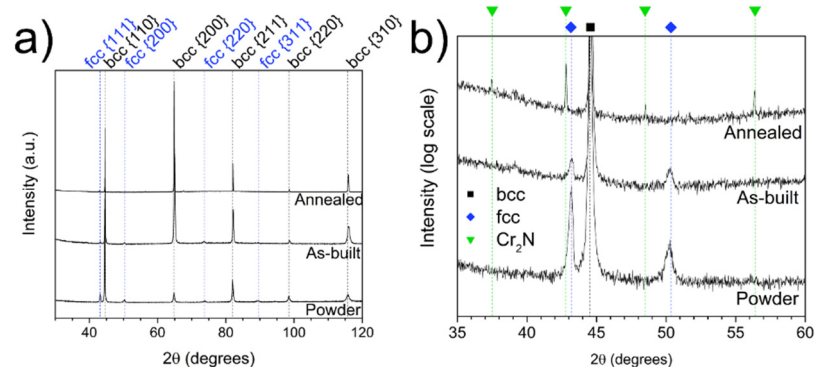

Figure 4. (**a**) XRD patterns of the feedstock powder, as-built and annealed samples. (**b**) XRD patterns shown with a logarithmic scale to emphasize the precipitating phases.

The XRD of the as-built and annealed L-PBF samples in Figure 4 also predominantly shows a ferritic phase, but additional peaks attributed to other phases could be observed. In the as-built sample, additional peaks can be seen attributed to the same austenitic phase as in the powder. Additionally, some preferential orientation could be seen along the <001> direction. The Orientation of the crystals along the build direction is common during the L-PBF processes and is a result of epitaxial growth during the partial remelting of previously deposited layers [27]. The annealing was performed by a two-step profile, using 1060 °C and 870 °C for 20 min and one hour, respectively. The samples were water-quenched between the two annealing steps and the final condition was obtained by air quenching from the last annealing temperature. The heat treatment procedure was chosen to be similar to conventionally produced SS446. The XRD pattern of the annealed sample (Figure 4) shows a ferritic phase in combination with Cr_2N, but without any fcc phase. The Cr_2N phase is expected to form during annealing according to the thermodynamic calculations shown in Figure 1. However, no indication of a carbide phase, as predicted by the calculations in Figure 2, was observed.

The phase compositions and unit cell parameters obtained from Rietveld refinements are summarized in Table 2. The amount of the austenite was estimated to be 14.2 wt.% and 4.6 wt.% in the powder and as-built sample, respectively. The decreased amount of the austenitic phase after printing can be explained by a loss of N during the L-PBF process, resulting in a less stable austenitic phase. The austenitic phase is not expected to form during solidification (see Figure 3), but is thermodynamically stable at equilibrium between 1000 °C and 1300 °C. This suggests that the austenitic phase may form due to solid-state phase transformations during the reheating of the material in the L-PBF process, as high temperatures are reached during the melting of subsequent layers. After annealing, the amount of the Cr_2N phase is estimated to be around 3.3 wt.% from the Rietveld refinements, which is close to the predicted amount at equilibrium. Furthermore, the amount of Cr_2N and austenite are similar in the printed samples. We observe that the phase fractions obtained from the thermodynamic calculations are at equilibrium and should thereby be used qualitatively and not quantitatively. The results, however, show that the thermodynamic calculations can be used as a powerful tool to increase the understanding and predict phase occurrence at various temperatures.

Table 2. Estimated amount of the phases and their cell parameters from Rietveld refinements.

	Phase Fraction (wt.%)			Unit Cell Parameter (Å)		
	bcc	fcc	Cr_2N	bcc	fcc	Cr_2N
Powder	85.8(8)	14.2(4)	-	a = 2.8761(1)	a = 3.6306(1)	-
As-built	95.4(9)	4.6(5)	-	a = 2.8732(1)	a = 3.6339(5)	-
Annealed	96.9(8)	-	3.3(3)	a = 2.8743(1)	-	a = 4.7999(1) c = 4.4520(7)

As austenite can dissolve a large amount of N in comparison to ferrite, it is suggested that Cr_2N can form close to the austenite phase or by precipitation due to the supersaturation of N in the ferrite phase during cooling. The lattice parameters of the ferrite, austenite and Cr_2N phases are listed in Table 2 and are normal for the Fe-based phases. The estimated size of the ferrite unit cell is similar for the different samples, suggesting that no large chemical variation of the ferrite occurs when forming austenite or Cr_2N.

Figure 5 shows EBSD orientation maps of the as-built SS446 ferritic stainless steel. The grain size varies within the sample, with some large grains reaching a diameter of close to 100 μm. These grains are surrounded by regions with smaller grains with sizes of up to around 10 μm. The larger grains adopt a cuboid shape (see Figure 5b), and an anisotropy in the grain morphology perpendicular and parallel to the build direction can be seen, with long columnar-shaped grains along the build direction. Several grains are oriented as <001> along the build direction, in agreement with the peak intensities from XRD. This type of microstructure has been seen in many materials produced by L-PBF

and is due to an epitaxial growth during the partial remelting of previously deposited layers [27]. The EBSD analysis shows that the austenitic phase can be present either at the grain boundaries (seen in box marked 1 in Figure 5b) or inside the ferrite grains (seen in box marked 2 in Figure 5b). Figure 5c,d shows the EBSD orientation and phase maps from box 1 with the austenite only at grain boundaries, while Figure 5e,f shows corresponding maps from box 2 with the austenite growing inside the ferrite grain. The precipitates at the grain boundaries have a more random orientation, while the precipitates inside the grains grow with a specific orientation in relation to the ferrite, and the EBSD analysis showed a coherency between the ferrite and the austenite, with [111]$_{ferrite}$ ∥ [110]$_{austenite}$. This relationship is commonly seen between ferrite and austenite in duplex stainless steels and is known as the Kurdjmov–Sachs (K–S) orientation relationship [28]. This kind of microstructure is expected to form in the solid-state and not during solidification [29]. Therefore, it is suggested that austenite is formed as a consequence of solid-state phase transformations taking place during the reheating of the material during the deposition of subsequent layers. However, further investigations would be needed to determine the exact mechanism for the formation of the austenitic phase in the L-PBF samples.
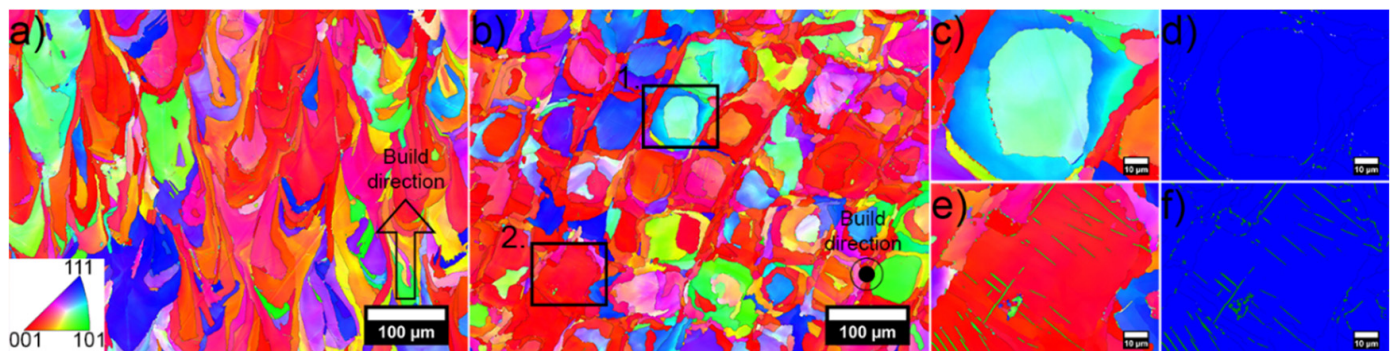

Figure 5. EBSD analysis of the as-built SS446 ferritic stainless-steel showing (**a**) EBSD orientation map along the build direction, (**b**) EBSD orientation map perpendicular to the build direction. The build direction is marked with an arrow in the images. (**c**,**d**) Show EBSD orientation map and phase map (ferrite in blue and austenite in green) of region 1 in (**b**). (**e**,**f**) show EBSD orientation map and phase map (ferrite in blue and austenite in green) of region 2 in (**b**).

Figure 6a shows a bright field (BF) STEM image of the as-built sample perpendicular to the build direction. A large number of dislocations can be seen, forming a cellular pattern with a distance of a few hundred nanometers. Furthermore, some precipitates were observed in these cell boundaries, which were enriched in Cr and N according to EDS (not shown here). The Z-contrast image in Figure 6b shows a grain boundary between two ferrite grains (marked with a black arrow). An austenitic precipitate (marked with a blue color) can be seen at the grain boundary. The phases are confirmed by the selected area electron diffraction (SAED) patterns shown in Figure S1 in the Supplementary Material. The EDS maps show an enrichment of Cr and N at the grain boundaries and in the austenitic precipitate. Furthermore, small spherical grains with a diameter of 20–40 nm can be seen inside the ferrite grains. EDS shows that they are enriched in Cr and O, suggesting the formation of oxides during solidification. This agrees with the Scheil–Gulliver calculations in Figure 3, wherein small amounts of an oxide with a spinel crystal structure are predicted to form during solidification. The particles observed in the TEM image in Figure 6b are therefore attributed to this phase (but not yet experimentally confirmed).
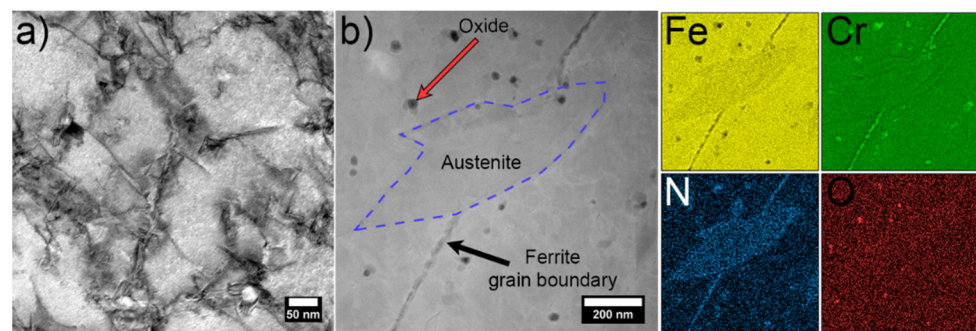
Figure 6. (**a**) BF STEM image of as-built SSS446 showing a high concentration of dislocations; (**b**) STEM Z-contrast image with a grain boundary and an austenite precipitate marked with blue dashed lines. The spinel grains within the ferrite grains are marked with a red arrow. Corresponding EDS maps are shown to the right.

As described earlier, small amounts of high-melting phases that solidify in the melt can act as nucleation agents and promote small grain sizes in FSSs due to enhanced heterogeneous nucleation [6,9,26]. This was observed in SS441 manufactured under similar conditions where the grain size in the as-build SS441 samples was only around 2 μm. The small grain size was explained by the presence of a corundum phase and TiN, which act as nucleation agents [6,7]. The large grain sizes observed in SS446 suggest that the spinel phase formed during solidification does not have the same effect on the nucleation behavior as the corundum phase and TiN. This can be explained by comparing the mole fraction of oxides and TiN in the two steel grades at temperatures close to the melting point. As seen in Figure 3, the Scheil–Gulliver calculations suggest that the amount of corundum/TiN in SS441 could be more than 30 times higher than the amount of spinel in SS446. The higher concentration of potential nucleation sites as well a previous study showing that spinel is a less efficient nucleation site for ferrite than, i.e., TiN [30], can explain the observed differences in grain size between SS441 and SS446.

Annealing experiments were performed in order to obtain a thermal history comparable to the conventionally produced alloy. EBSD orientation maps are shown in Figure 7. The grains remain elongated in the build direction, as shown in Figure 5, with a preferential orientation in the <100> direction, in agreement with the XRD results. The cuboid-like microstructure perpendicular to the build direction (Figure 7b) is similar as the one before the annealing step. Hence, no grain growth or recrystallization was observed from the EBSD analysis of the annealed samples. No austenite could be observed in the samples after annealing, which agrees with the phase fraction diagram shown in Figure 2. Some larger precipitates are observed at the grain boundaries of the ferrite. They are identified as Cr_2N, which is expected to form during annealing according to the thermodynamic calculations, shown in Figure 2 and observed in the XRD pattern in Figure 3. The phase map in Figure 7c confirms that Cr_2N with a size of a few μm is formed at the grain boundaries, but it could also be found inside the ferrite grains.

Figure 8 shows a TEM BF image of a cross-section parallel to the build direction. The lamella was extracted from a region within one of the ferrite grains. A decrease in dislocation density compared to the as-built material can be seen, as the dislocations are healed during annealing. Furthermore, some precipitates, enriched in Cr and N, have formed within the ferritic grains. These are assigned to the Cr_2N phase. The precipitation of nitrides can occur by the supersaturation of N during rapid cooling from high temperatures (quenched-in nitrides), or by isothermal heat treatments in the stability range of the nitride. The quenched-in nitrides are expected to form in the interior of the ferrite grains, while the isothermal nitrides form mainly at the grain boundaries where the diffusion rates of both N and Cr are high [31]. The nitrides observed in the annealed SS446 alloy are thereby suggested to originate from both of these processes. The formation of Cr_2N will induce

local variations in the chemical composition of the steel, which may be detrimental for the corrosion properties. The corrosion behavior was, however, outside the scope of this study.
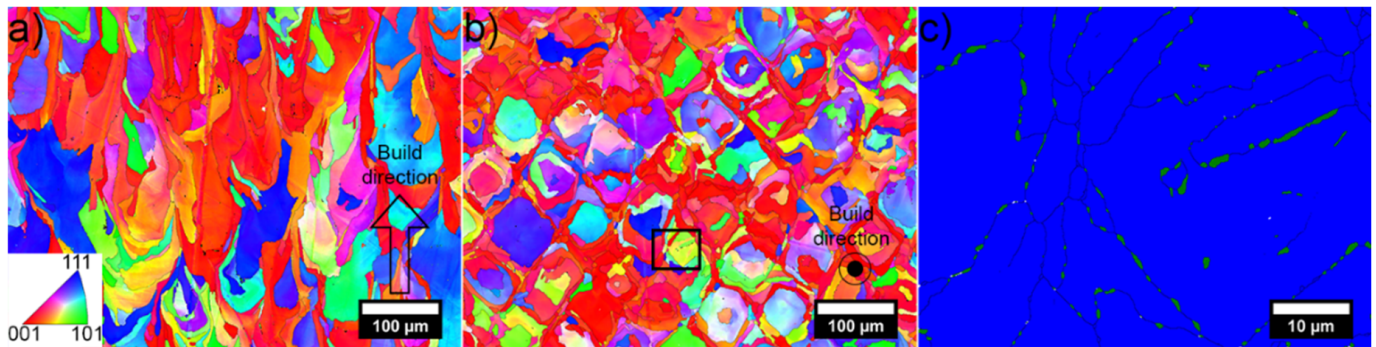

Figure 7. EBSD analysis of the annealed SS446 ferritic stainless-steel showing (**a**) EBSD orientation map along the build direction, (**b**) EBSD orientation map perpendicular to the build direction. The build direction is marked with an arrow in the images. (**c**) Shows EBSD phase map (ferrite in blue and Cr_2N in green) of the region marked with a black square in (**b**).
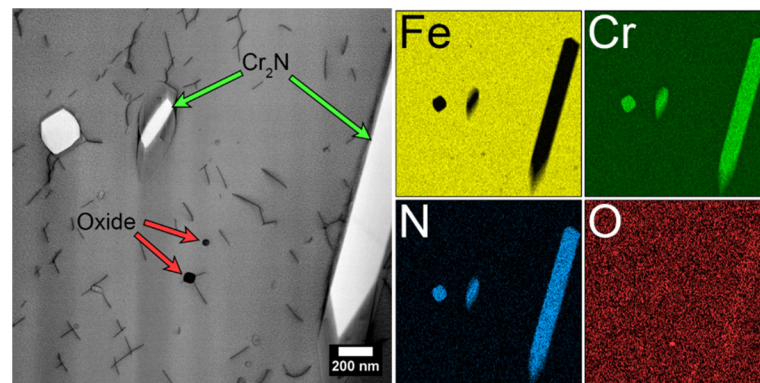

Figure 8. TEM of the annealed SS446 ferritic stainless-steel, showing a BF STEM image and corresponding EDS maps for Fe, Cr, N and O. The black lines in the STEM image are likely dislocations in the ferrite.

The mechanical properties of the as-built, annealed and reference SS446 FSS were investigated by tensile tests at room temperature. The resulting stress–strain curves are shown in Figure 9a. The as-built alloy shows a yield strength of around 950 MPa for the horizontally built samples, with a lower yield strength of around 840 MPa for the vertically built samples. All samples reached a similar elongation at fracture (around 20%). The anisotropic properties parallel and perpendicular to the build direction are reasonable due to the differences in the microstructure (see Figure 5). This kind of anisotropic properties are commonly seen in materials produced by L-PBF due to the formation of columnar grains, resulting in a different number of grain boundaries and thereby hardening in different directions in the sample. Upon annealing, the yield strength decreases drastically to 360 MPa and 342 MPa for the test directions perpendicular and parallel to the build direction, respectively, while the elongation at fracture increases to 25–30%. Both the yield strength and elongation of the annealed L-PBF samples are similar to the conventionally produced SS446. The greatly enhanced properties of the as-built material are associated with the presence of an austenitic phase in the large ferrite grains, as shown in Figure 5c–f. These precipitates in combination with the high dislocation density (Figure 6) are suggested to be responsible for the high yield strength by introducing a large number of obstacles that hinder the dislocation movement and strengthen the alloy. The healing of the dislocations and the introduction of large Cr_2N precipitates during annealing will significantly impact the properties, resulting in a more ductile material at the expense of strength.
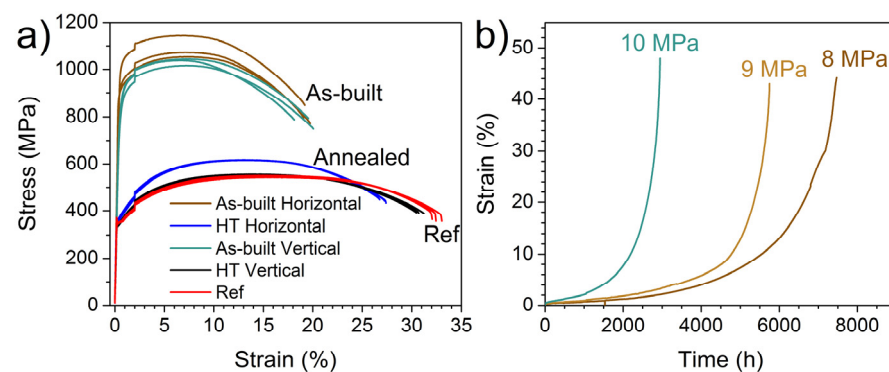
Figure 9. Mechanical properties of the SS446 ferritic stainless-steel showing (**a**) tensile stress–strain curves for the as-built annealed and reference samples and (**b**) creep curves for the L-PBF annealed sample.

The results suggest that the FSSs reported in this study reach an even higher yield strength (950 MPa vs. 741 MPa) than the previously reported SS441 alloy with excellent mechanical properties. The elongation, however, is lower in the reported alloy (20% vs. 30%). The yield strength is significantly reduced in the annealed state for SS446 compared to SS441 (360 MPa vs. 545 MPa), suggesting that the fine-grained microstructure obtained in earlier studies is important for the properties. Furthermore, the results indicate that the dislocation network seen in L-PBF-produced materials is of uttermost importance for the excellent mechanical properties.

The results from the creep tests of the L-PBF-produced SS446 FSSs are shown in Figure 9b. The creep strength of the conventionally produced SS446 is reported to be 10 MPa for 1000 h and 4.8 MPa for 10,000 h at 800 °C in [32,33]. The time to rupture at different stress levels for the L-PBF-produced material is shown in Table 3. The stress levels to rupture at 1000 h and 10,000 h are estimated to be 12.9 MPa and 7.7 MPa, respectively, which is significantly higher than the conventionally produced material. This indicates that the L-PBF-produced components possess an excellent creep resistance. The creep resistance is often improved by the large grain size of the alloy and it is therefore likely that the microstructure formed during L-PBF of SS446 FSSs is beneficial [34]. Precipitation of secondary phases at the grain boundaries or inside the grains have also been shown to enhance the creep behavior in FSSs [35]. Furthermore, the formation of coherent hierarchical microstructures could contribute to higher creep resistances in ferritic alloys [36]. It is therefore suggested that the formation of Cr_2N in this study plays an important role in the creep resistance of SS446 FSS.

Table 3. Creep data showing the time to rupture and elongation for different stress levels.

Stress (MPa)	Time to Rupture (h)	Elongation at Rupture (%)
10	2946	48
9	5751	43
8	7470	44
7.7 *	10,000	N/A
12.9 *	1000	N/A

* Extrapolated values assuming a linear relation between log (stress) and log (time to rupture).

Figure 10a shows the microstructure of the annealed SS446 alloy before any testing. The elongated microstructure along the build direction is visible (also shown in the EBSD images in Figure 7), with the precipitation of Cr_2N in the grain boundaries. Figure 10b,c shows micrographs of the sample after creep testing at 10 MPa close to the threads and the fracture surface, respectively. The region shown in Figure 10b is outside of the gauge of the specimen and the material has therefore experienced a minimal load but was heated to 800 °C for the duration of the test (around 3000 h). The long exposure at this temperature

promotes the growth of the Cr_2N precipitates in the grain boundaries. The microstructure of the ferrite, however, remains similar to the one before the long exposure at elevated temperatures. In the part of the sample that was exposed to an external load, a large number of pores are seen (Figure 10c) close to the grain boundaries. Inside the pores, the formation of Cr-rich oxides and nitrides could be detected by EDS (not shown here). Furthermore, the morphology of the ferrite is significantly altered close to the fracture surface and indicates a recrystallization occurring due to the induced stresses in combination with the high temperature during the creep tests. In contrast to these results, Calderón et al. found that the creep behavior of L-PBF-produced 316L samples was worse than those of the conventionally produced material by hot-rolling [37]. The creep damage of the L-PBF-produced samples was shown to be mainly intergranular and directly connected to the columnar microstructure due to unfavorably oriented grain boundaries (45° from load direction). Furthermore, the cellular structure plays and important role in the creep mechanisms due to the segregation of elements to the cell walls. The differences in the behavior of the FSSs presented in this study may be explained by the prior annealing experiments, initiating a recovery of dislocations, and promoting a favorable microstructure for creep. Furthermore, the more randomly oriented grain boundaries (especially close to the fracture where a recrystallisation has taken place, Figure 10c) results in a stronger creep behavior for L-PBF-produced SS446.
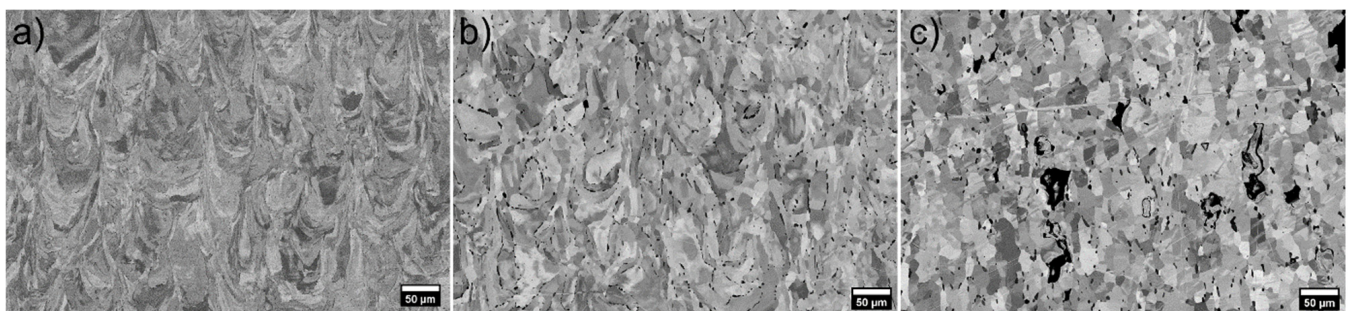

Figure 10. (**a**) SEM image of the heat-treated sample used for creep tests. (**b**,**c**) Show images after the creep tests in a region without and with load, respectively.

5. Conclusions

The components of the ferritic stainless steel SS446 can be successfully produced by L-PBF with outstanding mechanical properties and creep resistance. In order to mitigate cracking and produce high-quality samples with low porosity, a heating stage is required. An austenitic phase was observed in the powder and as-built material, where it forms in the grain boundaries of the ferrite as well as needle-shaped precipitates within the ferrite grains of the L-PBF samples. The coherency of the austenite phase, in combination with a high dislocation density, is theorized to significantly contribute to the excellent mechanical properties in the as-built samples.

The annealing of the alloy produces a nitride, Cr_2N, due to the isothermal heating in the stability range and the supersaturation of N in the ferrite during cooling. The Cr_2N precipitates at the ferrite grain boundaries and inside the grains were shown to be detrimental for the tensile properties. Additionally, the local depletion of Cr surrounding the Cr_2N precipitates implies a local reduction in corrosion resistance.

Thermodynamic calculations were used to model and monitor the phase stabilities and segregation during solidification. It is concluded that thermodynamic calculations can therefore be an important tool to support the design of new microstructures of high-Cr ferritic stainless steels. It should be noted that small fluctuations of the chemical composition in the calculations can have a large impact on the phase stabilities, and this effect illustrates the importance of controlled chemistry during the L-PBF process.

The tensile properties of the as-built material reach a yield strength of 950 MPa, almost three times that of the conventionally produced reference material by hot extrusion.

Furthermore, the creep tests indicate a stress of 7.7 MPa to obtain a fracture at 10,000 h, about twice as high as the reported values of the conventionally produced material.

In summary, this study shows that high-performing SS446 ferritic stainless steel can be produced by L-PBF with promising properties, enabling the design of new components with high performance. In order to improve the properties of the alloy even further, it is important to control the solidified microstructure, which could be performed by, e.g., introducing heterogeneous nucleation sites to obtain an equiaxed grain structure or by modifying the printing condition.

References

1. Davis, J.R. *Metals Handbook Desk Edition*, 2nd ed.; ASM International: Materials Park, OH, USA, 1998.
2. Cortie, M.; Du Toit, M. Stainless steels, ferritic. In *Reference Module in Materials Science and Materials Engineering*; Elsevier: Amsterdam, The Netherlands, 2016; ISBN 978-0-12-803581-8.
3. Sello, M.P.; Stumpf, W.E. Laves phase embrittlement of the ferritic stainless steel type AISI 441. *Mater. Sci. Eng. A* **2010**, *527*, 5194–5202. [CrossRef]
4. DebRoy, T.; Wei, H.L.; Zuback, J.S.; Mukherjee, T.; Elmer, J.W.; Milewski, J.O.; Beese, A.M.; Wilson-Heid, A.; De, A.; Zhang, W. Additive manufacturing of metallic components—Process, structure and properties. *Prog. Mater. Sci.* **2018**, *92*, 112–224. [CrossRef]
5. Jiang, P.F.; Zhang, C.H.; Zhang, S.; Zhang, J.B.; Chen, J.; Chen, H.T. Additive manufacturing of novel ferritic stainless steel by selective laser melting: Role of laser scanning speed on the formability, microstructure and properties. *Opt. Laser Technol.* **2021**, *140*, 107055. [CrossRef]
6. Durga, A.; Pettersson, N.H.; Malladi, S.B.A.; Chen, Z.; Guo, S.; Nyborg, L.; Lindwall, G. Grain refinement in additively manufactured ferritic stainless steel by in situ inoculation using pre-alloyed powder. *Scr. Mater.* **2021**, *194*, 113690. [CrossRef]
7. Karlsson, D.; Chou, C.-Y.; Pettersson, N.H.; Helander, T.; Harlin, P.; Sahlberg, M.; Lindwall, G.; Odqvist, J.; Jansson, U. Additive manufacturing of the ferritic stainless steel SS441. *Addit. Manuf.* **2020**, *36*, 101580. [CrossRef]
8. Chou, C.-Y.; Karlsson, D.; Pettersson, N.H.; Helander, T.; Harlin, P.; Sahlberg, M.; Jansson, U.; Odqvist, J.; Lindwall, G. Precipitation kinetics during post-heat treatment of an additively manufactured ferritic stainless steel. *Metall. Mater. Trans. A* **2022**, *53*, 3073–3082. [CrossRef]
9. Ikehata, H.; Jägle, E. Evaluation of microstructure and tensile properties of grain-refined, Ti-alloyed ferritic stainless steel fabricated by laser powder bed fusion. *Mater. Sci. Eng. A* **2021**, *818*, 141365. [CrossRef]
10. Mally, L.; Werz, M.; Weihe, S. Feasibility study on additive manufacturing of ferritic steels to meet mechanical properties of safety relevant forged parts. *Materials* **2022**, *15*, 383. [CrossRef]
11. Mukherjee, T.; Zhang, W.; DebRoy, T. An improved prediction of residual stresses and distortion in additive manufacturing. *Comput. Mater. Sci.* **2017**, *126*, 360–372. [CrossRef]
12. Fang, Z.-C.; Wu, Z.-L.; Huang, C.-G.; Wu, C.-W. Review on residual stress in selective laser melting additive manufacturing of alloy parts. *Opt. Laser Technol.* **2020**, *129*, 106283. [CrossRef]

13. Sung, J.H.; Kong, J.H.; Yoo, D.K.; On, H.Y.; Lee, D.J.; Lee, H.W. Phase changes of the AISI 430 ferritic stainless steels after high-temperature gas nitriding and tempering heat treatment. *Mater. Sci. Eng. A* **2008**, *489*, 38–43. [CrossRef]

14. Pettersson, N.; Pettersson, R.F.A.; Wessman, S. Precipitation of chromium nitrides in the super duplex stainless steel 2507. *Met. Mater. Trans. A* **2015**, *46*, 1062–1072. [CrossRef]

15. Guimarães, A.A.; Mei, P.R. Precipitation of carbides and sigma phase in AISI type 446 stainless steel under working conditions. *J. Mater. Process. Technol.* **2004**, *155–156*, 1681–1689. [CrossRef]

16. Liu, M.; Tay, N.H.S.; Belusko, M.; Bruno, F. Investigation of cascaded shell and tube latent heat storage systems for solar tower power plants. *Energy Procedia* **2015**, *69*, 913–924. [CrossRef]

17. Zhang, H.; Su, H.; Hou, Y.; Wang, X.; He, Y.; Li, F. The microstructure evolution of equiaxed-to-columnar in compositionally graded samples from pure Fe to Fe-27 wt.%Cr fabricated by laser powder bed fusion. *Mater. Lett.* **2023**, *330*, 133255. [CrossRef]

18. Rietveld, H.M. A profile refinement method for nuclear and magnetic structures. *J. Appl. Crystallogr.* **1969**, *2*, 65–71. [CrossRef]

19. Rodríguez-Carvajal, J. Recent advances in magnetic structure determination by neutron powder diffraction. *Phys. B Condens. Matter* **1993**, *192*, 55–69. [CrossRef]

20. Kuhn, H.; Medlin, D. *Mechanical Testing and Evaluation*; ASM International: Materials Park, OH, USA, 2000; ISBN 978-1-62708-176-4.

21. Andersson, J.-O.; Helander, T.; Höglund, L.; Shi, P.; Sundman, B. Thermo-Calc & DICTRA, computational tools for materials science. *Calphad* **2002**, *26*, 273–312. [CrossRef]

22. Lukas, H.; Fries, S.G.; Sundman, B. *Computational Thermodynamics: The Calphad Method*, 1st ed.; Cambridge University Press: Cambridge, UK, 2007; ISBN 978-0-521-86811-2.

23. Thermo-Calc Software TCFE9: TCS Steel and Fe-Alloys Database 2020. Available online: https://www.thermocalc.com/media/10306/tcfe9_extended_info.pdf (accessed on 16 June 2021).

24. Gokuldoss, P.K.; Kolla, S.; Eckert, J. Additive manufacturing processes: Selective laser melting, electron beam melting and binder jetting—Selection guidelines. *Materials* **2017**, *10*, 672. [CrossRef]

25. Hooper, P.A. Melt pool temperature and cooling rates in laser powder bed fusion. *Addit. Manuf.* **2018**, *22*, 548–559. [CrossRef]

26. Shi, X.; Chang, L.; Zhou, L. Solidification structure refinement of ferritic stainless steel based on heterogeneous nucleation technology. *J. Iron Steel Res. Int.* **2019**, *26*, 137–147. [CrossRef]

27. Köhnen, P.; Létang, M.; Voshage, M.; Schleifenbaum, J.H.; Haase, C. Understanding the process-microstructure correlations for tailoring the mechanical properties of L-PBF produced austenitic advanced high strength steel. *Addit. Manuf.* **2019**, *30*, 100914. [CrossRef]

28. Kral, M.V. Proeutectoid ferrite and cementite transformations in steels. In *Phase Transformations in Steels*; Elsevier: Amsterdam, The Netherlands, 2012; pp. 225–275, ISBN 978-1-84569-970-3.

29. Chen, T.H.; Yang, J.R. Microstructural characterization of simulated heat affected zone in a nitrogen-containing 2205 duplex stainless steel. *Mater. Sci. Eng. A* **2002**, *338*, 166–181. [CrossRef]

30. Isobe, K. Effect of Mg addition on solidification structure of low carbon steel. *ISIJ Int.* **2010**, *50*, 1972–1980. [CrossRef]

31. Bettini, E.; Kivisäkk, U.; Leygraf, C.; Pan, J. Study of corrosion behavior of a 2507 super duplex stainless steel: Influence of quenched-in and isothermal nitrides. *Int. J. Electrochem. Sci.* **2014**, *9*, 61–80.

32. Alleima 4C54 High-Temperature Stainless Steel. Available online: https://www.Alleima.Com/Se/Products/Tube-Pipe-Fittings-and-Flanges/High-Performance-Materials/High-Temperature-Stainless-Steels/Sandvik-4c54/ (accessed on 7 November 2022).

33. ASM Handbook Committee (Ed.) *Properties and Selection: Irons, Steels, and High-Performance Alloys*; ASM International: Materials Park, OH, USA, 1990; ISBN 978-1-62708-161-0.

34. Cain, V. High Temperature Creep Behaviour Niobium Bearing Ferritic Stainless Steels. Master's Thesis, Cape Peninsula University of Technology, Cape Town, South Africa, 2005.

35. Jiang, M.; Han, Y.; Sun, J.; Sun, J.; Zu, G.; Chen, H.; Ran, X. Precipitation of Cu- and Nb-rich phases and its strengthening effect in 17Cr ferritic stainless steel during high-temperature creep process. *Mater. Charact.* **2021**, *179*, 111346. [CrossRef]

36. Song, G.; Sun, Z.; Li, L.; Xu, X.; Rawlings, M.; Liebscher, C.H.; Clausen, B.; Poplawsky, J.; Leonard, D.N.; Huang, S.; et al. Ferritic alloys with extreme creep resistance via coherent hierarchical precipitates. *Sci. Rep.* **2015**, *5*, 16327. [CrossRef]

37. Ávila Calderón, L.A.; Rehmer, B.; Schriever, S.; Ulbricht, A.; Agudo Jácome, L.; Sommer, K.; Mohr, G.; Skrotzki, B.; Evans, A. Creep and creep damage behavior of stainless steel 316L manufactured by laser powder bed fusion. *Mater. Sci. Eng. A* **2022**, *830*, 142223. [CrossRef]